

## Article

# The Effect of Ultrafine-Grained (UFG) Structure Formed by Equal-Channel Angular Pressing in AA7075 on Wear and Friction in Sliding against Steel and Ceramic Counterbodies

Andrey V. Filippov <sup>\*</sup>, Sergei Y. Tarasov  and Ekaterina O. Filippova 

Institute of Strength Physics and Materials Sciences Siberian Branch of Russian Academy of Science, Per. Akademicheskii 2/4, 634055 Tomsk, Russia; tsy@ispms.ru (S.Y.T.); katerinabosix@mail.ru (E.O.F.)

\* Correspondence: avf@ispms.ru

**Abstract:** The mechanical characteristics and sliding friction behaviors of AA7075 samples were studied in regard to structural states formed in them by ECAP and depending on the ECAP pass number. In addition, the effect of a counterbody's material on the tribological characteristics of the samples was investigated by the examples of AISI 52100 steel, alumina  $\text{Al}_2\text{O}_3$  and silicon nitride  $\text{Si}_3\text{N}_4$ . Vibration acceleration and acoustic emission signals with parameters such as acoustic emission energy and median frequency were used for characterizing the sliding regimes. The structural state and mechanical properties of the ECAPed AA7075 samples significantly affected their wear behaviors in dry sliding. The counterbody material had a significant influence on the formation of a transfer layer and the subsurface deformation of samples. The dynamic behavior of the tribosystem was studied and the relationship between the sliding parameters, vibrometry and acoustic emission signals was established.

**Keywords:** aluminum alloy; sliding friction; wear; severe deformation; structure



**Citation:** Filippov, A.V.; Tarasov, S.Y.; Filippova, E.O. The Effect of Ultrafine-Grained (UFG) Structure Formed by Equal-Channel Angular Pressing in AA7075 on Wear and Friction in Sliding against Steel and Ceramic Counterbodies. *Metals* **2024**, *14*, 527. <https://doi.org/10.3390/met14050527>

Academic Editor: Wenming Jiang

Received: 25 March 2024

Revised: 26 April 2024

Accepted: 29 April 2024

Published: 30 April 2024



**Copyright:** © 2024 by the authors. Licensee MDPI, Basel, Switzerland. This article is an open access article distributed under the terms and conditions of the Creative Commons Attribution (CC BY) license (<https://creativecommons.org/licenses/by/4.0/>).

## 1. Introduction

The aluminum 7075 alloy is used in many industries for making structures that demand high mechanical characteristics and low weight. Wear resistance is also an important characteristic of this alloy which enables one to expand the field of application. However, determining the wear resistance requires taking into account numerous factors and specific conditions including the type of contact, scheme of loading, sliding speed, ambient temperatures and environment. Changing only one of them would cause dramatic changes in wear and friction. Other important factors contributing to the wear resistance are the resistance of the material to deformation and fracture and its stability against structural and phase transformations induced by sliding factors such as subsurface deformation and frictional heating.

The effect of retrogression and reaging treatment on the wear of aluminum alloy 7075 was studied [1] in dry sliding against an  $\text{Al}_2\text{O}_3$  ball that demonstrated that the main wear mechanism was the adhesion transfer. Sliding in a solution 30 g/L NaCl + 10 g/L HCl showed that the wear was mainly caused by abrasion. Heat treatment affected the structure and phase composition of the samples, which in turn affected the wear resistance of the samples.

One of the specific features of sliding on ductile materials is the generation of mechanically mixed layers (MMLs) [2] that determine further evolution of the material, i.e., wear and friction. Once generated on the AA7075, the MML increased its wear resistance under dry-sliding friction conditions [3]. However, wear increased with the normal load, which may be caused by breaking the dynamic equilibrium between generation and deterioration of this MML. Elevating the ambient temperatures from 25 °C to 250 °C led to changing the wear mechanism from adhesive to oxidative and then even to extrusion (flow wear). It was

shown [4] that under sliding conditions, the 6 h aged state of AA7075 T6 demonstrated better wear resistance compared to the as-cast state and the AA7075 T6 alloy aged for 2 h. The results of this work show that normal load is the main factor to determine wear resistance, while both heat treatment and sliding speed are less important ones. However, it was reported elsewhere [5] that sliding distance had the greatest influence on wear, followed by load and sliding speed.

Changing the type of the relative motion between the sample and the counterbody may also have a significant impact on wear mechanisms. The worn surface formed on AA7075 by fretting wear was characterized by the presence of thin MML with cracks and damaged areas [6]. Earlier, it was revealed [7] that the use of a lubricant significantly changes the conditions of contact between AA7075 and a steel counterbody. The lubricated fretting resulted in wear by microplothing with wear particles.

Along with the abrasive wear and delamination, torsional fretting of AA7075 was characterized by oxidation of the worn surfaces, which contributed to less adhesion wear between the materials [8]. The dual-rotary fretting of AA7075 flat samples against the AISI 52100 steel balls allowed for the identification of the wear mechanisms such as abrasive wear, delamination and mild oxidative wear [9].

Previously, it was also reported [10] that severe plastic deformation with cracking was observed on the worn surface of AA7075 samples after decreasing the fretting displacement amplitude. The results of another work [11] showed that cracks were initiated at the contact area edges of AA7075 samples in fretting under mixed wear conditions. The formation of a protrusion as a result of plastic deformation of the aluminum alloy was also noted. Wear of AA7075 was less intensive in plain sliding as compared to that of in the sliding+fretting mode, where delamination, abrasive and oxidative wear were observed [12]. It was found [13] that higher humidity enhanced tribo-oxidation during fretting of AA7075 against the 52100 steel. The tribolayer generation was more intense, with moisture adsorbed on the contact surfaces that enabled a reduction in both friction and wear of the AA7075. The wear scar ends accumulated oxidized wear particles as a result of torsional fretting on the AA7075 [14]. Increasing the torsional fatigue stress resulted in a gradual increase in the coefficient of friction (CoF), wear scar depth and degree of the worn surface oxidation.

Performance testing of an oil casing made of AA7075 demonstrated that formation of tribo-oxide layers is a key protection mechanism [15]. Increasing the sliding speed initially increased the thickness of this layer, but if the sliding speed was too high, this layer became unstable and was easily removed from the alloy surface.

One approach to increasing the wear resistance of AA7075 is to improve its mechanical properties by means of various types of impact treatment. For instance, shot peening of AA7075-T651 improved its resistance against adhesive wear under dry-sliding conditions [16]. At the same time, the CoF of the shot-peened AA7075-T651 increased, which was explained by subsurface hardening and more intensive formation of anti-adhesion oxide films.

Laser surface texturing was also used to improve the wear resistance of AA7075 [17]. The treatment resulted in hardening the surface, which allowed for a reduction in the intensity of plastic deformation and adhesion.

The outspread application of materials modified using severe plastic deformation (SPD) methods posed a question as to whether or not this ultrafine-grained structural state would provide improvements in wear resistance and numerous studies have been undertaken to elucidate this issue. It was reported [18,19] that the wear mechanism changed from adhesive to oxidative and was the main reason for an improvement in the wear resistance on ultrafine-grained AA7075 compared to that of the coarse-grained state. However, no information was provided about the wear of the counterbodies (steel balls), which would be important when analyzing the adhesive wear. These works also indicate that the plastic deformation penetrates deeper into coarse-grained annealed material as compared to that of the fine-grained one because of reduced adhesion and higher strength.

As a result of studying the cross section metallographic views of AA7075 samples after sliding, it was found that equal-channel angular pressing (ECAP) provided a hardening effect and thus allowed for a reduction in the penetration of plastic deformation [20]. It was also noted [21] that ECAP enabled an increase in the CoF and, simultaneously, reduced wear on an Al-Zn-Mg alloy under dry-sliding conditions. At the same time, it was pointed out that an adhesive wear mechanism took place and delamination was observed under the action of friction force.

A significant enhancement in both strength and hardness with corresponding grain refinement [22] was provided after 1 to 6 ECAP passes on AA7050 at room temperature. The more ECAP passes, the greater the effect on increasing the CoF and reducing the wear. The impaired ductility due to ECAP contributed to reducing the effects of adhesion and delamination of the material. Similar observations were reported for AA7075 [23].

During dry-sliding friction of AA7075 paired with an Al<sub>2</sub>O<sub>3</sub> ball [24], the CoF and specific wear rate of AA7075 increased after ECAP despite the increased hardness. The increase in wear rate was due to the formation of oxide wear particles, which acted as an abrasive [24].

It is not always possible to improve both the strength of AA7075 by ECAP and its wear resistance in dry-sliding conditions. For example, ECAP of as-cast AA7075 increased its hardness to 100–120 HV [25], which is a relatively low value in comparison with the above-discussed results. However, these samples demonstrated a high wear rate when rubbed against a stainless steel ball compared to that of a AA7075 T6 aged sample.

The majority of the above-discussed studies were dedicated to comparing wear resistances and wear mechanisms between coarse-grained and ultrafine-grained materials. It is known that effective grain refinement may be achieved only after several SPD passes that usually also require inter-pass heating. Only multi-pass SPD allows for significant modification of both the structural state of the material and improvements in its physical and mechanical properties [26–28]. At the same time, dynamic recrystallization is needed to form high-angle grain boundaries after several ECAP passes and, therefore, preheating is necessary. It is also known that SPD served to enhance the wear resistance of commercially pure titanium [29], titanium alloy Ti6Al4V [30,31] and magnesium alloys AZ31B [32], AZ91 [33], Mg–2 wt%Y–0.6 wt%Nd–0.6 wt%Zr [34] and Mg–4Li [35].

Therefore, the influence of the ECAP pass number on grain refinement and then on the tribological behaviors of thus modified materials may be either positive or negative. By the example of ECAPed brass, it was shown [36] that three-pass ECAP resulted in subsurface fracture during sliding friction. At the same time, the first ECAP pass proved to be the most effective for improving both the mechanical strength and wear resistance of the ECAPed brass.

Determining the influence of the structural state of the material on the sliding behavior and wear of the material is a complex and important task. In addition, special attention should be paid to assessing the impact of the counterbody on the wear and the sliding friction dynamics. In this regard, the purpose of this work was to study the influence of the structural states obtained after different numbers of ECAP passes on the sliding of AA7075 against counterbodies made from dissimilar materials.

## 2. Materials and Methods

ECAP was carried out using the Bc scheme with 90° angle revolution around the sample's axis on cylindrical samples machined from the hot-rolled AA7075 bar, annealed at 475 °C for 180 min for overaging and achieving the level of ductility acceptable in the ECAP (Figure 1a). The ECAP die was preheated to 100 °C before processing and then this temperature was maintained during further processing of the samples at a pressing rate of 100 mm/s. Each ECAP pass corresponded to 100% strain. The following four types of samples have been used in this research: (1) as-annealed, (2) 1-pass ECAPed, (3) 2-pass ECAPed, and (4) 4-pass ECAPed.

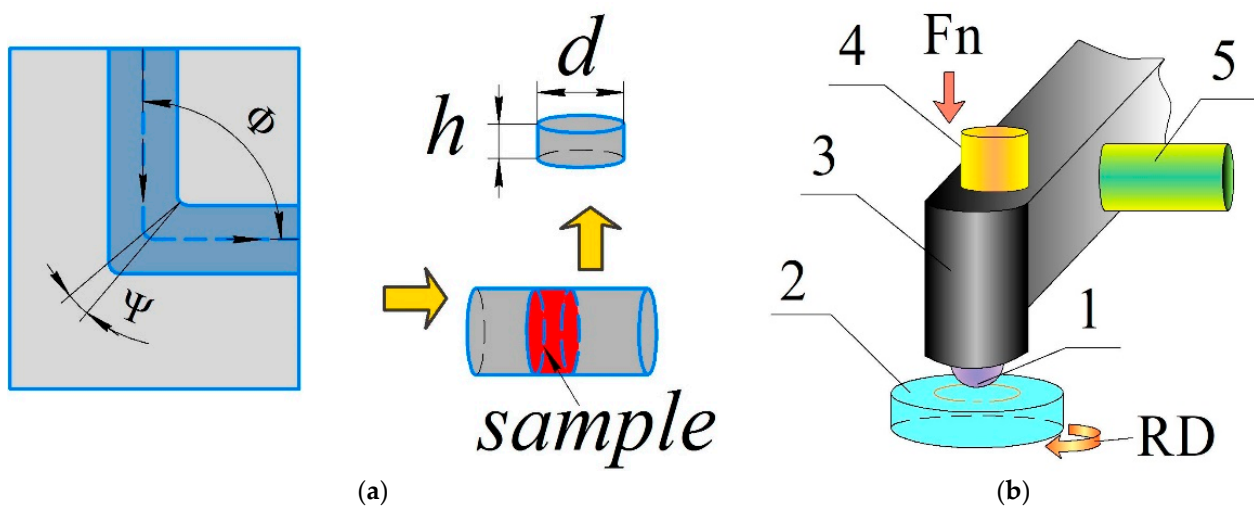


**Figure 1.** ECAP die geometry and sample preparation scheme (a); sliding test scheme with AE and VA sensors (b). 1—counterpart (ball), 2—AA7075 disk, 3—AE sensor, 4 and 5—vibration sensors.

The grain and sub-grain structures formed in these samples after corresponding treatments were characterized by means of a TEM instrument *JEM-2100* (JEOL Ltd., Tokyo, Japan) on thin foils prepared from disks cut off the cylindrical sample in the plane perpendicular to its axis (Figure 1) using an EM-09100IS (JEOL Ltd., Tokyo, Japan) sample preparation system. Phase detection in samples after ECAP and sliding tests were performed using a Shimadzu XRD-7000S X-ray diffractometer (Shimadzu, Kyoto, Japan). The mechanical characteristics (tensile test) of the samples were acquired using a Testsystems 110M-10 (Testsystems, Ivanovo, Russia) test machine at ambient temperatures. Each datapoint was obtained by averaging over three experimental results.

The ECAPed sample's hardness was measured using a nanohardness Nano Hardness Tester NHT-S-AX-000X CSEM (CSEM Instruments, Neuchatel, Switzerland) at normal load 100 mN on the sample surfaces polished to  $R_a = 0.05 \mu\text{m}$ . Samples (disks) intended for tribological testing were machined from the ECAPed AA7075, bars as shown in Figure 1a, ground and polished to achieve a roughness of  $R_a = 1.25 \mu\text{m}$ .

Sliding experiments were carried out according to the ball-on-disk scheme (Figure 1b) at 20 N normal load and sliding velocity 0.1 m/s, which were implemented using a *Tribotechnic tribometer* (Tribotechnic, Clichy, France). Three different types of  $\varnothing 6$  mm balls were used, made from (1) quenched and tempered ball bearing AISI 52100 steel, (2) alumina ( $\text{Al}_2\text{O}_3$ ) and (3) silicon nitride ( $\text{Si}_3\text{N}_4$ ). The use of counterpart specimens made from different materials was intended for studying the effect of adhesion transfer on sliding regimes, which were characterized by in situ registering both acoustic emission (AE) and vibration acceleration (VA) signals. The AE signals were received and then treated using an EYa-1 equipment (Togliatti State University, Tolyatti, Russia). The AE signal parameters such as median frequency and signal energy were then computed from the AE signal waveform according to [8] and then used for characterization of the sliding regimes. The vibration acceleration signals were registered by means of an IMI industrial accelerometer and USB data logger NI-9234 (National Instruments, Austin, TX, USA) at a sampling rate of 25.6 kHz. The running root mean square (runRMS) of acceleration was calculated for 1 s signal acquisition periods. The AE and VA sensors were mounted on the tribometer arm (Figure 1b, position 4-5).

The wear track surfaces and profiles were examined by means of laser scanning microscope Olympus OLS LEXT 4100 (Olympus, Tokyo, Japan). An SEM instrument *NIKKISO SM3000* (NIKKISO, Tokyo, Japan) attached with an EDS add-on was used for studying the worn surfaces. No less than 3 samples were used for obtaining each datapoint in the sliding tests.

### 3. Results

#### 3.1. Microstructure, Phase Composition and Mechanical Properties

The ECAP die is an efficient tool for grain–subgrain structure refinement by severe plastic deformation (SPD) so that  $\sim 700$  nm size grains were obtained after one-pass ECAP (Figure 2a with inset). These grains contain dislocations and therefore give the SAED reflections with noticeable azimuthal misorientations. The two-pass ECAP formed banded grain structures with high-angle boundaries separating these grains from each other (Figure 2b). These banded grains with an aspect ratio of 0.2:1  $\mu\text{m}$  demonstrated their SAED reflections with a higher degree of azimuthal misorientation (Figure 2b, inset). Fine, 250–300 nm, size grains were formed after the four-pass ECAP with SAED reflections characterized by wider azimuthal misorientation (Figure 2c), which, in addition to dislocation density, might be a result of further grain refinement, i.e., 50 nm dynamically recrystallized grains that were surrounded by intermetallic precipitates.

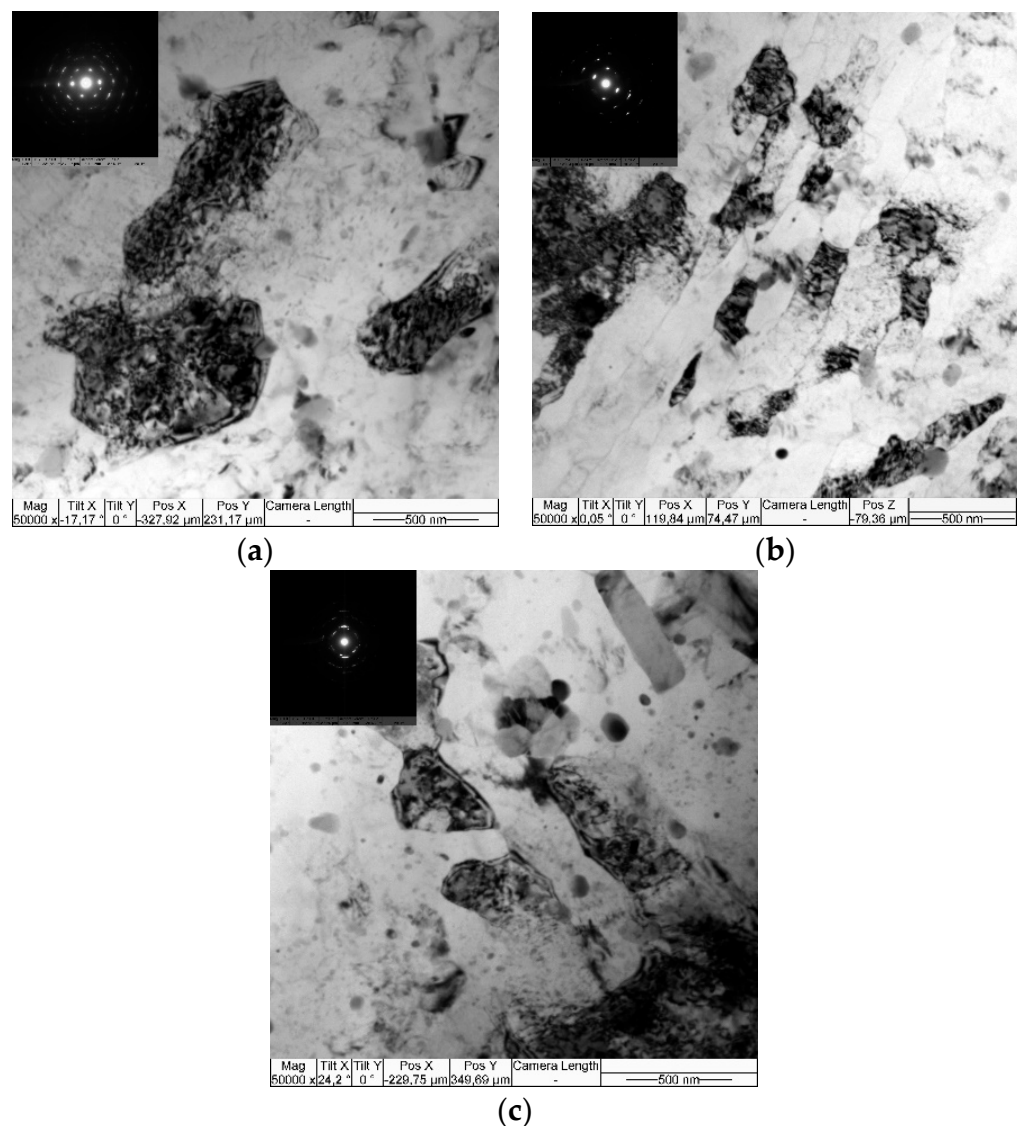


**Figure 2.** TEM images of AA7075 grain structures after 1- (a), 2- (b) and 4- (c) pass ECAP.

The phase compositions of all samples were elucidated by means of X-ray diffractometry, which demonstrated the main reflections from  $\alpha$ -Al solid solution, which was the base metal in all the cases (Figure 3). The as-annealed sample was also characterized by the presence of reflections from S-phase ( $\text{Al}_2\text{CuMg}$ ) particles that probably precipitated and coarsened during heating to 475 °C.

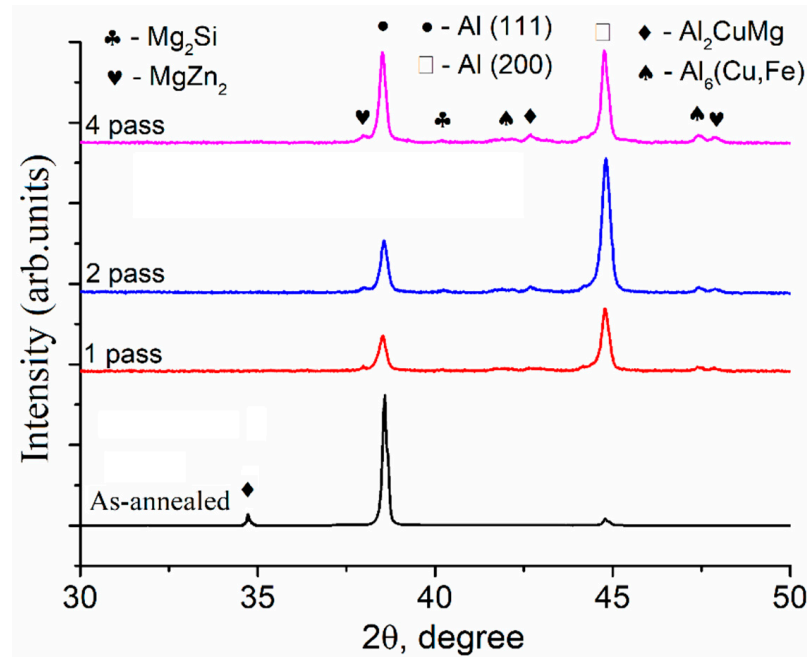


Figure 3. X-ray diffractograms from as-annealed and ECAPed AA 7075 samples.

XRD of the samples after ECAP allowed us to identify phases such as the  $\eta$ -phase ( $\text{MgZn}_2$ ),  $\text{Mg}_2\text{Si}$ , and  $\text{Al}_6(\text{Cu,Fe})$ , along with those mentioned above. These precipitates are commonly found in aluminum alloys of the composition Al–Zn–Mg–Cu [37]. The  $\alpha$ -Al solid solution lattice parameter for as-annealed and ECAPed samples changed as follows:  $4.0534 \text{ \AA} \rightarrow 4.0343 \text{ \AA} \rightarrow 4.0491 \text{ \AA} \rightarrow 4.0470 \text{ \AA}$ .

It may be assumed that the one-pass ECAP is accompanied by fragmentation and strain dissolution of particles earlier precipitated in annealing, which resulted in reducing the lattice parameter because of the formation of a solid solution with Zn, Mg and Cu atoms that have atomic radii smaller than that of aluminum. The two-pass ECAP resulted in somewhat increasing the lattice parameter, which may be related to the precipitation of fine reinforcement particles. Finally, the lattice parameters reduced again after the four-pass ECAP, which suggests dissolution of these particles.

The mechanical characteristics of the materials are determined by hardening mechanisms that might contribute to the mechanical strength and plasticity levels of AA7075 samples: (1) grain refinement according to the Hall–Petch law, (2) dispersion hardening by coherent intermetallic precipitates, and (3) solid-solution hardening. The precipitates capable of providing the effect of dispersion hardening of AA7075 include coherent  $\eta'$  ( $\text{MgZn}_2$ ) particles, which usually grow from Guinier–Preston (GP) zones nucleated in the supersaturated solid solution during aging. Therefore, the above-discussed in terms of lattice parameter change situations with precipitation and dissolution of precipitates may be related to evolution of mechanical characteristics depending on the ECAP pass number.

Tensile testing and the nanoindentation method were used for determining the mechanical characteristics of the samples (Figures 4 and 5). The results of the testing showed that the as-annealed metal possessed low yield strength (YTS) and ultimate tensile stress (UTS) levels corresponding to those of AA7075 after T6 heat treatment. In addition, this sample is characterized by the highest plasticity, which, of course, is the result of overaging the reinforcement particles.

Higher values of both YTS and UTS have been obtained after one-pass ECAP as compared to that of the as-annealed sample (Figures 4 and 5). The same behavior was observed for the elasticity modulus obtained from the nanoindentation according to the Oliver–Pharr method. The level of nanohardness, however, increased to 153 HV (Figure 4). This sample also possessed a plasticity lower than that of the as-annealed sample (Figure 5). The improvements in both tensile UTS and YTS after one-pass ECAP may be related to

grain refinement and solid-solution hardening, which is determined by dissolution of alloying elements in  $\alpha$ -Al, which is observed by the lattice constant decrease from 4.0534 Å to 4.0343 Å (Figure 4).

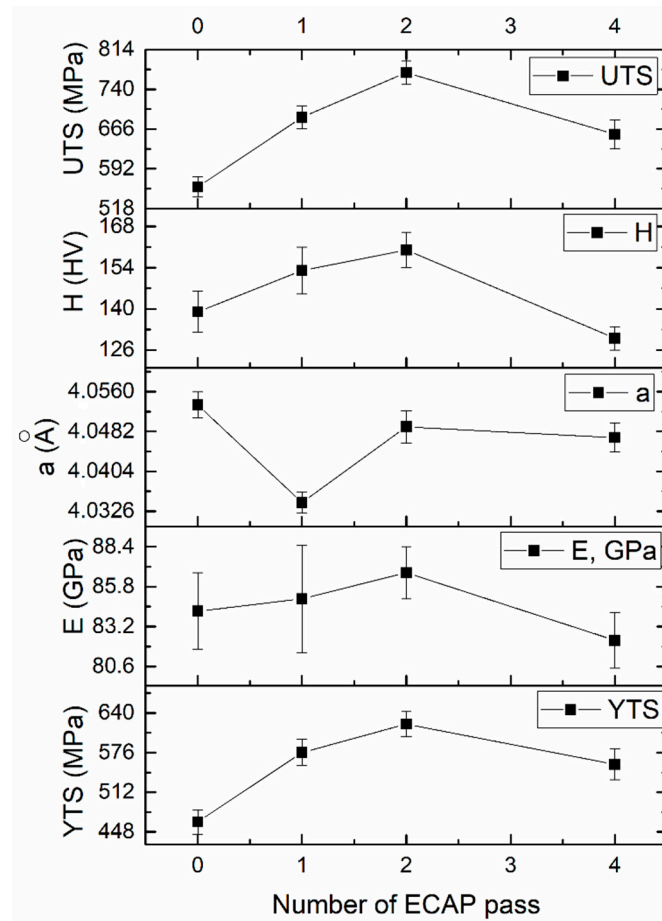


Figure 4. Lattice parameter and mechanical characteristics of the annealed and ECAPed AA7075 vs. ECAP pass number.

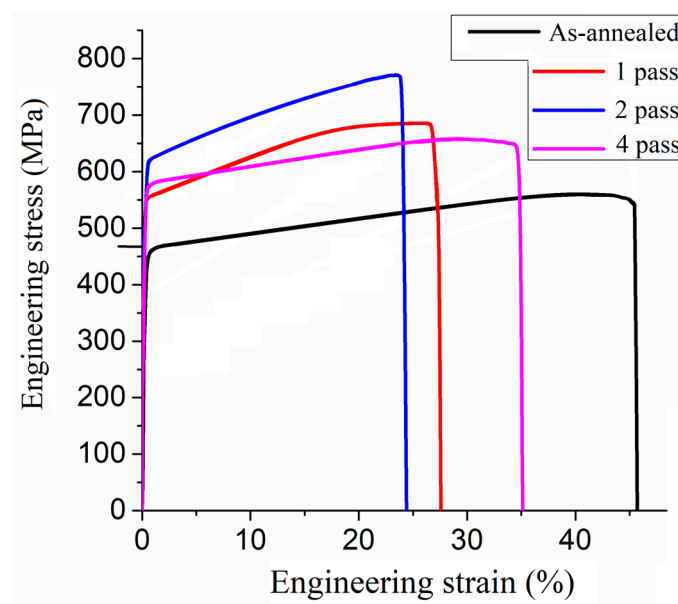
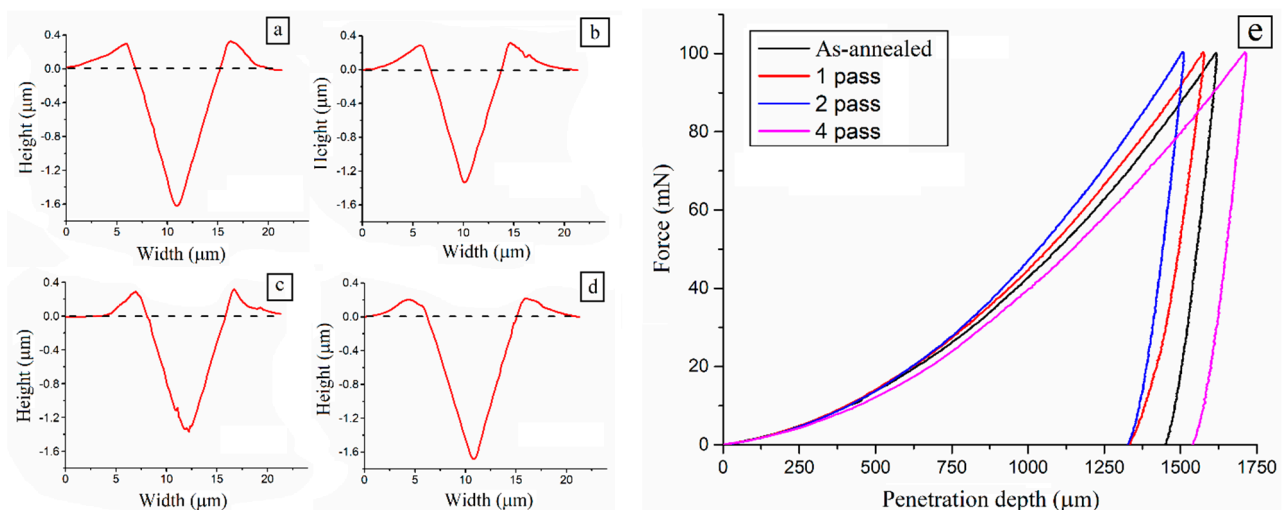


Figure 5. Typical tensile curves for as-annealed and ECAPed AA7075 samples.

The highest YTS, UTS, and elasticity modulus, as well as nanohardness numbers, further increased after two-pass ECAP due to the more efficient grain refinement and dispersion hardening (Figure 4). The latter coincides with the lattice parameter growth to 4.0491 Å. In addition, the elasticity modulus increased as compared to that after one-pass ECAP. The plasticity of this sample was minimal (Figure 5).

The four-pass ECAP resulted in some small degradation of mechanical characteristics such as UTS, YS, and elasticity modulus, as compared to those obtained after two-pass ECAP (Figure 4). However, there was an improvement in the plasticity characteristic (Figure 5). Plausibly, this may be an effect of over-deforming and growth of either non-coherent or semi-coherent precipitates, as well as recrystallization [38–40]. One reason may also be the anisotropy of mechanical characteristics due to the presence of deformation texturing, the existence of which follows from observing the X-ray peak heights in Figure 3.

When measuring the nanohardness with the Vickers pyramid, it was noticed that there are bulges at the perimeter of the indentation that form by pushing out the ductile metal by the downward moving pyramid. These bulges are known as pile-ups and their profiles can be obtained using confocal laser microscopy, as seen in Figure 6a–d, together with the corresponding indentation loading curves (Figure 6e). The pile-up height can be adopted as characteristic of metal's ductility at the micrometer scale. Therefore, their geometry was described as a ratio between the pyramid penetration depth ( $h_c$ ) to its maximum value ( $h_{max}$ ). The variation in the  $h_c/h_{max}$  is related to the variation in mechanical characteristics of the metal at the microscale, caused, for instance, by the grain refinement. Considering how this ratio varies with the ECAP pass number may also be helpful to gain a better understanding of the interplay between microscale deformation and overall strengthening of the material (Figure 7). It follows from analyzing the data in Figure 7 that despite ECAP providing hardening, noticeable plastic metal flow may occur near the pyramid, so all samples except the four-pass ECAP one show high  $h_c/h_{max}$  and pile-up heights. The reduced  $h_c/h_{max}$  and pile-up height on the four-pass ECAP sample may be caused by its higher ductility, resulting from easier recrystallization of over-deformed grains (Figure 6c). The loading four-pass curve in Figure 6e also testifies in favor of this suggestion regarding the higher ductility of this sample. It is worthwhile to note that similar behaviors of pile-ups were reported elsewhere for ECAPed brass [36].



**Figure 6.** Nanoindentation profiles from as-annealed (a) and 1-pass (b), 2-pass (c) and 4-pass (d) ECAPed AA7075 samples. Nanoindentation curves (e).

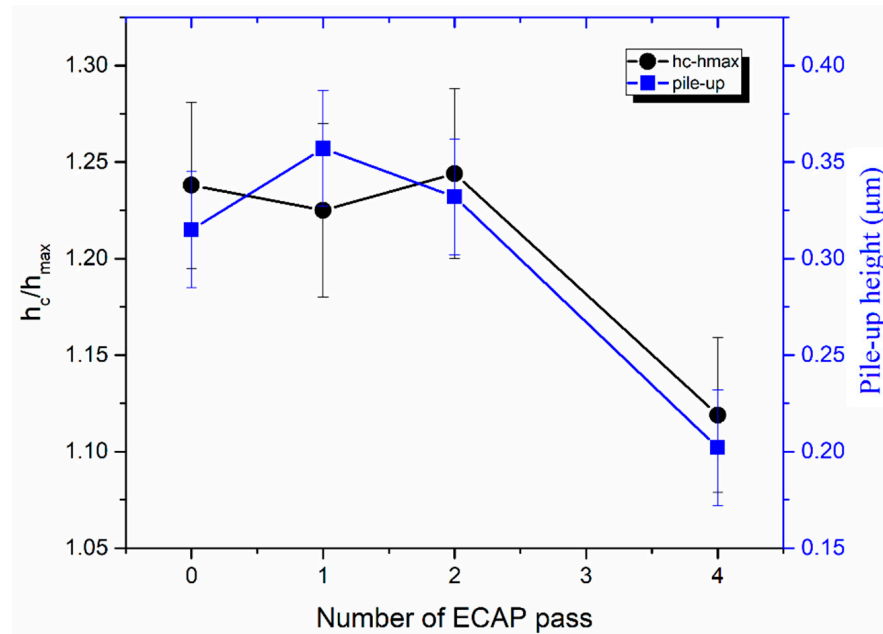


**Figure 7.** The effect of ECAP passes on the  $h_c/h_{max}$  ratio and pile-up heights.

### 3.2. CoF, Vibration and Acoustic Emission

Tribological testing enabled us to observe that the coefficient of friction (CoF) was oscillating in the range of  $\sim 0.11$  to  $\sim 0.23$  for both steel and alumina balls rubbed against the samples (Figure 8a). The CoF's mean values were within the 0.16–0.18 range. A somewhat lower friction was observed in sliding with the  $\text{Si}_3\text{N}_4$  ball, which may be explained from the dynamics of sliding and adhesion of this ball with respect to AA7075. The dynamics of sliding may be inferred from the in situ measurements of the vibration accelerations (VA). The VA amplitudes measured in sliding on the two-pass ECAP sample are 25–75% higher than those obtained from sliding on the as-annealed sample with either steel or silicon nitride or alumina balls, respectively (Figure 8b). The VA amplitude is increased also for all ECAPed samples compared to that of the as-annealed sample, with small enhancement of the VA signal in sliding on the one-pass ECAP sample, the maximum on the two-pass one and, again, somewhat reduced values on the four-pass sample. The minimum VA amplitudes were achieved with the alumina ball, while the maximum ones corresponded to sliding with the steel one. The silicon nitride ball produced VA amplitudes close to those obtained in sliding the one-pass ECAP sample against the steel. However, the VA amplitudes corresponding to sliding ceramic balls against both two-pass and four-pass ECAP AA7075 samples are lower than those obtained in sliding against the steel.

The above-discussed results suggest that in situ VA signal changes were occurring during sliding and may be then related to adhesion wear and transfer of the metal [41–43].

It was discovered earlier [44–47] that AE characteristics such as median frequency and energy are the most informative ones when used for studying fast-occurring processes such as metal cutting, where friction is an integral feature. The mean values of these characteristics are convenient means for assessing the sensitivity of the wear and friction to the structural states of the materials in rubbing, as demonstrated by the results shown in Figure 9. For instance, high values of AE signal's energy generated from sliding alumina balls against the AA7075 samples (Figure 8a) corresponded to the lowest median frequencies (Figure 8b). When sliding the silicon nitride balls, the values of AE signal energy reduced and even became minimal in sliding the AA7075 samples against the steel balls. The minimal sensitivity of the AE signal energy to structural state of the AA7075 samples was detected when using the silicon nitride balls.

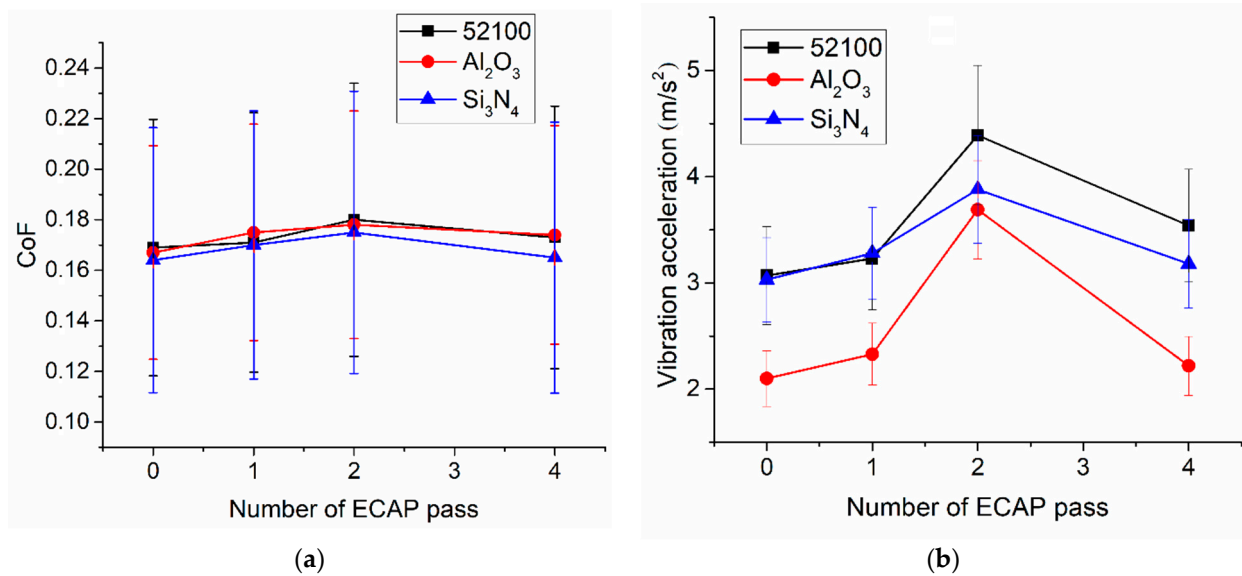


**Figure 8.** The effect of ECAP pass number and counterbody material on coefficient of friction (a) and vibration acceleration (b).

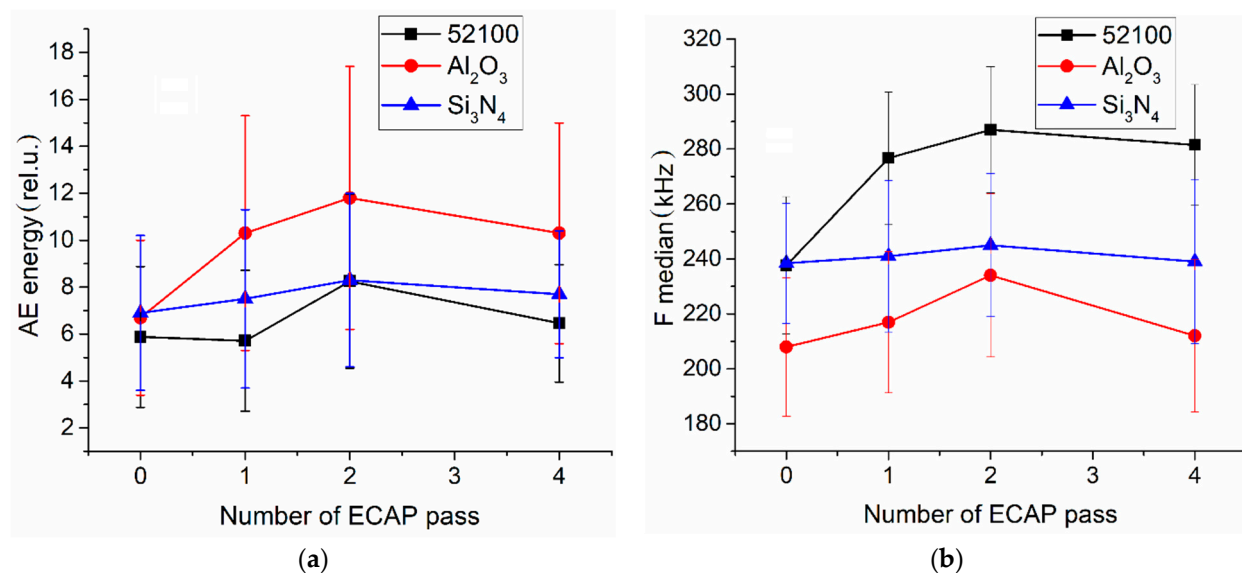


**Figure 9.** The effect of ECAP pass number and counterbody material on acoustic emission median frequency (a) and energy (b).

When it comes to seeking a relationship between the AE characteristics and ECAP passes performed, the maximums of the AE characteristics fall upon the two-pass ECAP sample, similarly to the behaviors of the VA amplitudes.

The increase in median frequency was related to domination of brittle fractures and, vice versa, median frequency reduced in viscous fractures [48]. As soon as the mechanical characteristics of the samples are determined by their microstructures resulting from the ECAP, their deformation and fractures in the sliding test may be monitored by means of AE signals.

### 3.3. Worn Surface and Adhesion Transfer Layer Thickness

#### 3.3.1. Confocal Laser Scan Study of AA7075 Worn Surface and Counterbody Surface

The worn surfaces of all disk samples and balls were examined with the use of confocal optical microscopy. Transferred layers of an aluminum alloy in the form of bright

regions were observed on the surface of the balls, together with dark tribooxidized regions (Figure 10). The maximum amount of adhesion-transferred metal was observed on the silicon nitride ball, less on the alumina ball, and the minimum on the steel ball. All micrographs show uneven distribution of transferred metal on the balls' surface, which is typical with the adhesion transfer from the sample to the ball and back to the sample [49].

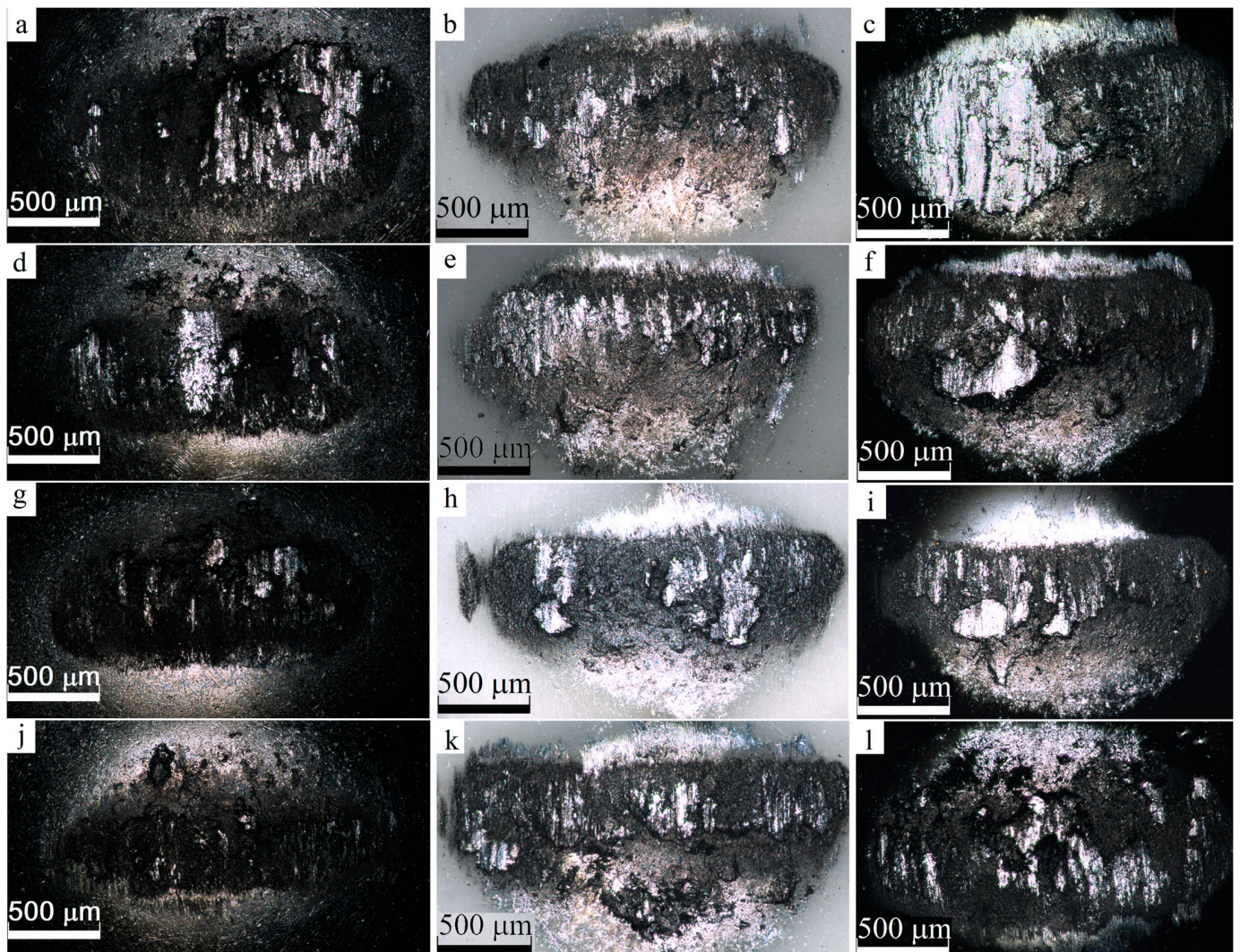


**Figure 10.** Optical micrographs of the worn surfaces on the 52100 steel (a,d,g,j),  $\text{Al}_2\text{O}_3$  (b,e,h,k) and  $\text{Si}_3\text{N}_4$  (c,f,i,l) balls covered with metal transferred from the samples. As-annealed (a–c), 1-pass (d–f), 2-pass (g–i), 4-pass (j–l) AA7075.

The wear of the AA7075 samples and amount of metal transferred to the ball were quantized by reconstructing the cross section area of the wear track and transfer built-up on the ball, respectively (Figure 11). The microstructural states formed by ECAP in the AA7075 demonstrated a reduction in wear compared to that of the as-annealed sample (Figure 12a). When it comes to comparing the effect of ECAP passes on wear, the minimal wear value was obtained on the two-pass ECAP sample rubbed against the steel ball. The ceramic balls demonstrated almost the same wear values on this sample. Sliding on the four-pass ECAP sample resulted in some wear enhancement as compared to that of the two-pass sample, especially in sliding with the alumina ball, while using the steel one gave minimal enhancement.

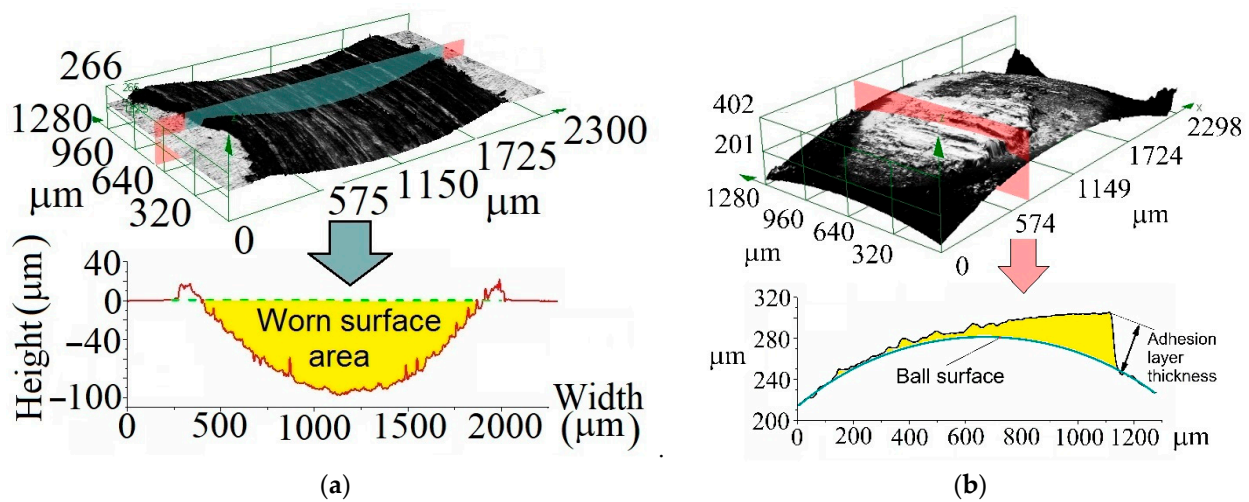


Figure 11. Measuring wear (a) and adhesion transfer layer thickness (b).

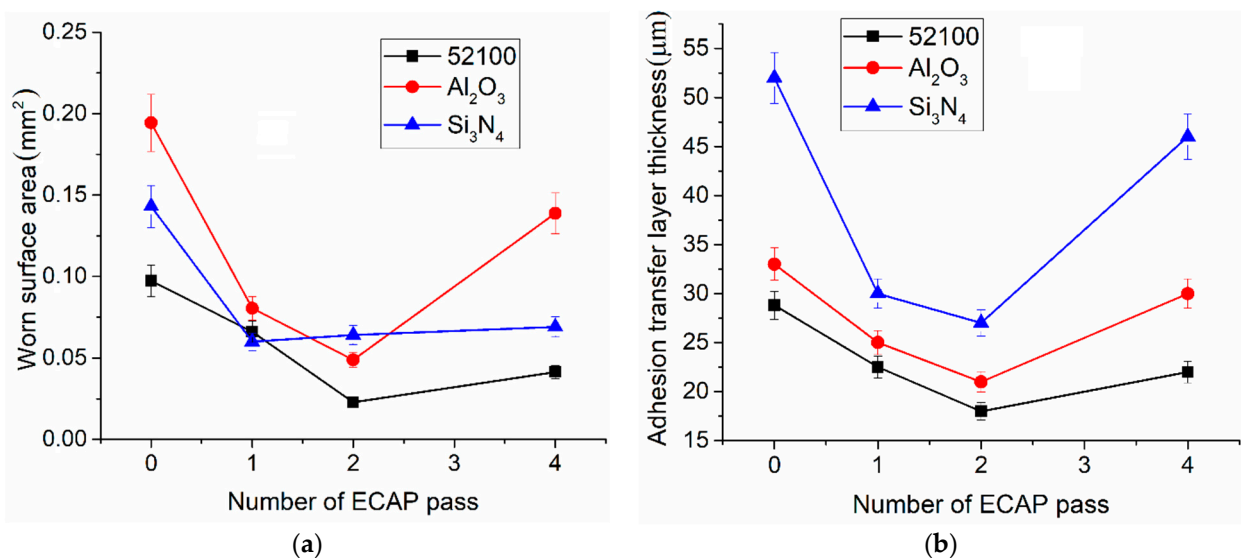


Figure 12. Effect of ECAP pass number and counterbody material on worn surface area (a) and adhesion transfer layer thickness (b).

Quantization of the transferred metal amounts was carried out by measuring the transfer layer maximum thickness along the ball's radius (Figure 11b). These measurements were plotted then vs. the ECAP pass numbers and types of the balls used (Figure 12b). The dependencies similar to those characterizing the wear were observed (Figure 12b), i.e., low wear values corresponded to low amounts of transferred-to-ball metal and vice versa. However, in terms of the types of the balls, the transfer layer amounts reduced, starting from those on the silicon nitride ball to those on the alumina and steel for all ECAP pass numbers used.

Strong bonding between aluminum and ceramics, i.e., Al/Al<sub>2</sub>O<sub>3</sub> and Al/Si<sub>3</sub>N<sub>4</sub>, may be achieved under conditions of high pressure and at elevated temperatures, as reported [50,51]. These conditions are commonly observed when opposite asperities contact each other in unlubricated sliding and thus produce real contact spots characterized with the temperature flashes. Therefore, the transfer of metal onto ceramic-surface balls in sliding is inevitable. It is more likely that no strong chemical bond is formed between the metal and ceramics under these conditions, but it may really happen with increasing both the contact pressure and temperature [49].

These data also establish a relationship between the transfer layer thickness and AE characteristics, i.e., an increase in the transfer thickness corresponds to a reduction in the AE characteristics. The same relationship may be established between wear and AE characteristics. It is important to note, however, that the thicker the transfer layer, the less the changes in these AE characteristics are manifested (Figure 9). The AE signal emitted from the subsurface of the AA7075 sample fades within this layer and, therefore, its characteristics tend not to change even if the structural state of the sample changes. Under these circumstances, the contribution from fracture and transfer layer generation to the AE signal would be more essential compared to that of subsurface plastic deformation.

### 3.3.2. SEM Study of AA7075 Worn Surfaces

Sliding on metals is commonly accompanied by subsurface layer deformation, grain refinement and oxidation, which may result in the generation of a subsurface modified layer. Such a tribological layer is subjected to fracture and adhesion transfer, which define the wear and friction of the metal. The wear tracks formed on the as-annealed samples by the steel balls demonstrate wear particles that result from adhesion sticking and transfer of metal (Figure 13). The damaged areas can be observed on the worn surfaces of both two-pass and four-pass ECAP samples, which form due to subsurface fracture and adhesion transfer of the metal. Smooth areas might be formed by sliding over the tribooxidized tribological layer, which has less adhesion to the steel ball.

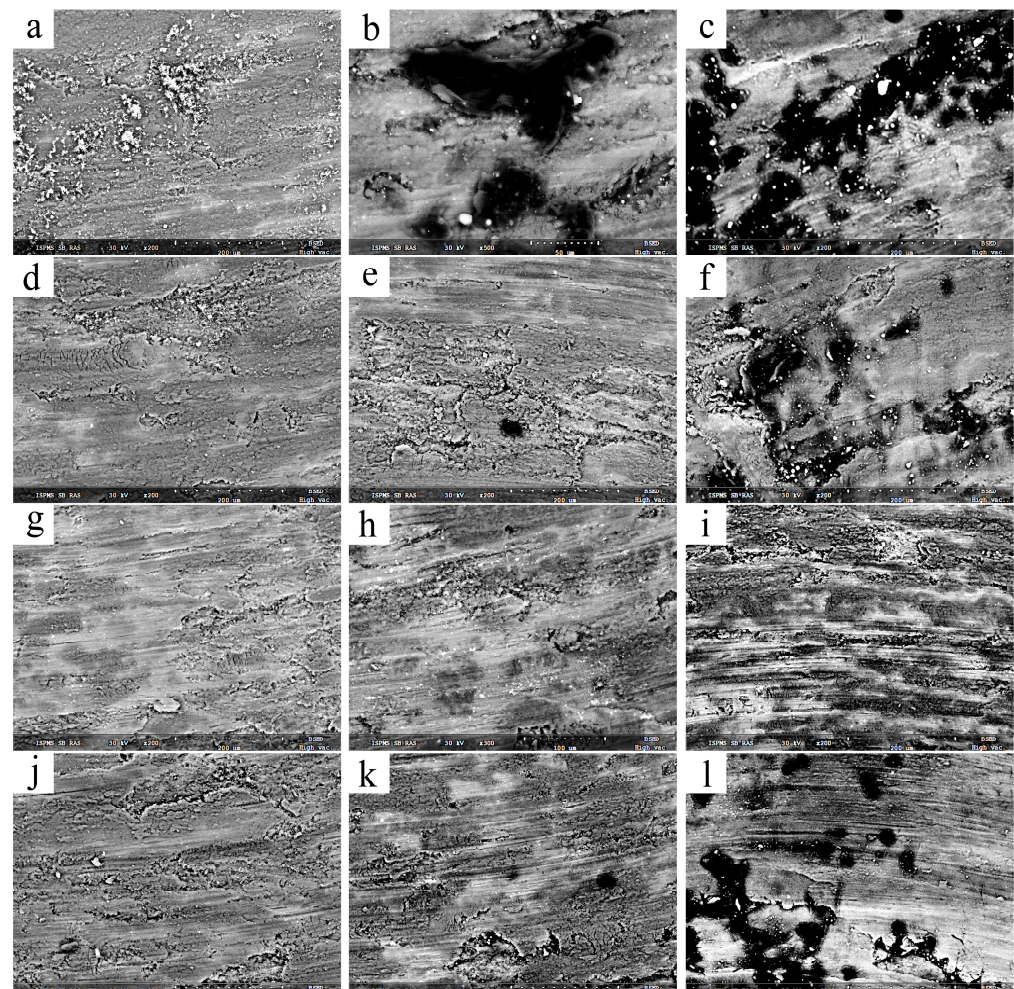


**Figure 13.** SEM BSE images of the wear track surfaces on AA7075 samples obtained in sliding with 52100 steel (a,d,g,j),  $\text{Al}_2\text{O}_3$  (b,e,h,k) and  $\text{Si}_3\text{N}_4$  (c,f,i,l) balls. As-annealed (a–c), 1-pass (d–f), 2-pass (g–i), 4-pass (j–l) AA7075.

Sliding between AA7075 and the ceramic balls resulted in the formation of the wear track on the as-annealed sample, whose surface was covered by dark areas with high oxygen concentrations (Figure 13). These dark areas are present on the as-annealed sample rubbed against the alumina ball, while the worn surfaces of the ECAPed samples are almost free of them. More intensive adhesion of AA7075 to the silicon nitride balls caused more intense adhesion wear of the AA7075 samples, including those subjected to ECAP. Taking into account the fact that these balls are characterized by more amounts of transferred AA7075 metal, these dark areas might have resulted from pulling out and adhesion transfer of the metal onto the ball surface.

The EDS spectra have been obtained from the worn surfaces of all samples that testify that tribooxidation is an essential factor in sliding on the AA7075 and therefore all the worn surfaces are characterized by high concentrations of oxygen (Tables 1–3). The mean concentration of iron on the worn surfaces resulting from sliding by the steel ball is at the level of its concentrations on the worn surfaces obtained with ceramic balls. Therefore, no iron was transferred from the steel ball to the AA7075 surfaces.

**Table 1.** EDS spectra from the worn surfaces of AA7075 samples obtained in sliding with the 52100 steel.

Sample State	Counterbody		Steel Ball 52100					
	Chem. elem. wt. %	O	Mg	Al	Si	Fe	Cu	Zn
	Spectrum Number							
As-annealed	1	14.5	1.2	76.5	1.4	0.5	1.3	4.6
	2	36.9	1.8	54.1	1.2	1.2	1.0	3.8
	3	24.5	1.6	58.1	3.5	1.6	3.4	7.3
1-pass ECAP	1	41.2	1.6	43.6	3.0	3.4	4.9	2.3
	2	32.9	0.4	63.0	1.0	0.1	2.2	0.4
	3	53.3	1.1	41.3	1.4	0.6	1.4	0.9
2-pass ECAP	1	32.5	0.8	63.8	0.9	0.2	1.6	0.2
	2	23.1	0.6	70.0	1.1	1.0	3.6	0.6
	3	24.1	1.4	65.5	2.1	0.8	5.2	0.9
	4	36.7	0.9	60.5	0.3	0.1	1.4	0.1
4-pass ECAP	1	41.6	0.8	53.8	0.9	1.0	1.4	0.5
	2	39.9	1.1	54.6	0.7	0.7	2.1	0.9
	3	33.3	1.7	58.2	1.5	1.5	2.9	0.9
	4	40.5	1.1	53.0	1.3	1.1	2.3	0.7

**Table 2.** EDS spectra from the worn surfaces of AA7075 samples obtained in sliding with the Al<sub>2</sub>O<sub>3</sub>.

Sample State	Counterbody		Ceramic Ball Al <sub>2</sub> O <sub>3</sub>					
	Chem. elem. wt. %	O	Mg	Al	Si	Fe	Cu	Zn
	Spectrum Number							
As-annealed	1	35.0	0.4	60.6	1.8	0.4	1.2	0.6
	2	11.5	1.5	71.0	7.4	2.2	4.7	1.7

Table 2. Cont.

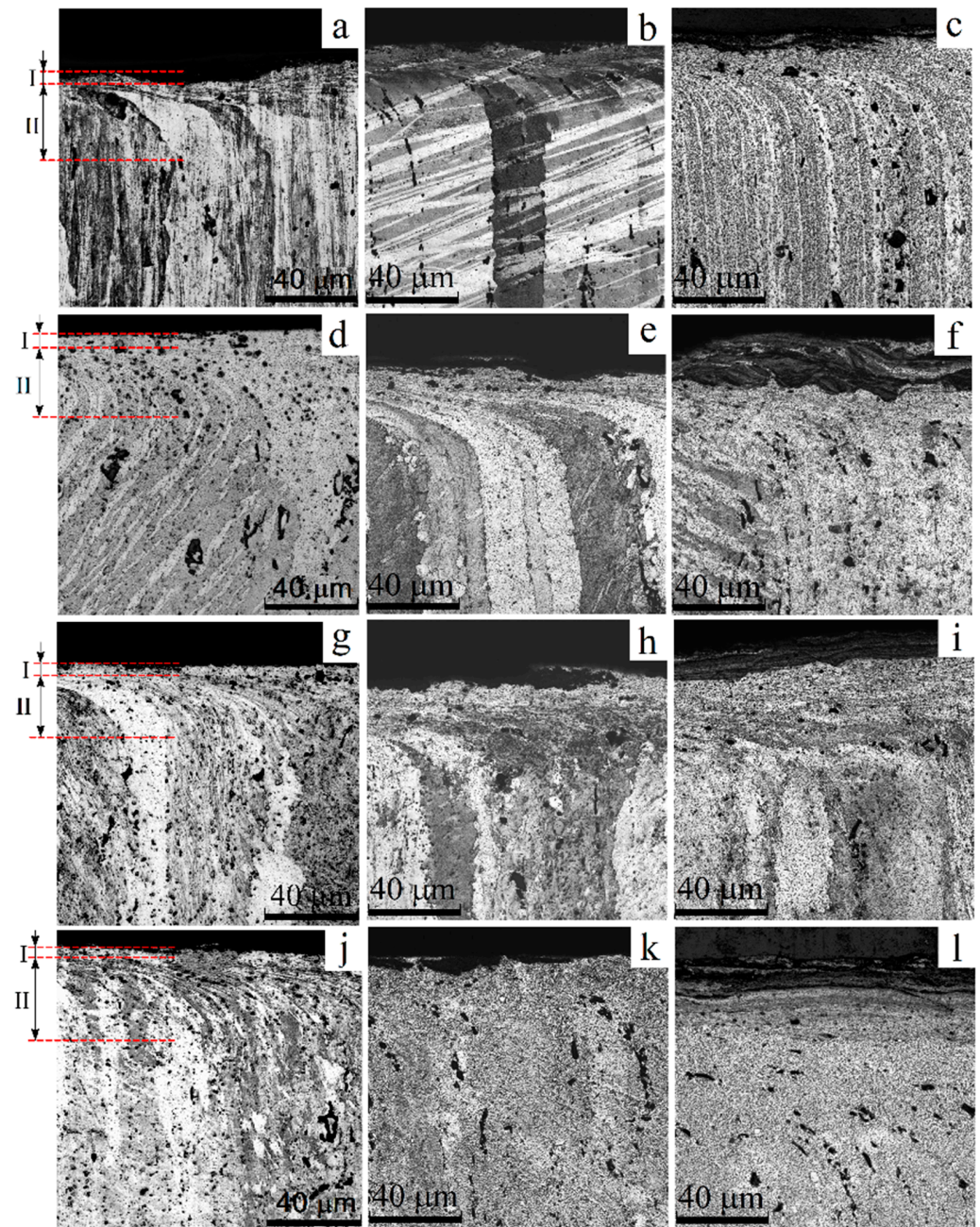
Sample State	Counterbody		Ceramic Ball Al <sub>2</sub> O <sub>3</sub>					
	Chem. elem. wt. %	O	Mg	Al	Si	Fe	Cu	Zn
	Spectrum Number							
1-pass ECAP	1	28.6	0.7	65.4	1.3	0.4	2.7	0.9
	2	42.5	0.4	55.3	0.1	0.4	1.1	0.2
	3	37.8	0.9	57.9	0.5	0.4	2.2	0.3
	4	37.8	1.0	58.4	0.5	0.4	1.7	0.2
	5	24.9	0.8	72.4	0.2	0.2	1.4	0.1
	6	39.3	1.2	57.4	0.4	0.2	1.3	0.2
2-pass ECAP	1	9.4	0.9	85.1	1.7	0.4	2.1	0.4
	2	38.4	1.0	56.7	1.6	0.3	1.4	0.6
	3	12.2	1.6	70.5	5.0	1.6	6.5	2.6
4-pass ECAP	1	33.3	0.4	62.9	0.8	0.3	2.1	0.2
	2	45.5	0.4	49.5	2.7	0.2	1.2	0.5
	3	46.0	0.3	50.8	1.2	0.2	1.3	0.2
	4	29.6	0.7	66.9	0.9	0.1	1.6	0.2
	5	39.4	0.9	55.4	2.2	0.3	1.5	0.3

Table 3. EDS spectra from the worn surfaces of AA7075 samples obtained in sliding with the Si<sub>3</sub>N<sub>4</sub>.

Sample State	Counterbody		Ceramic Ball Si <sub>3</sub> N <sub>4</sub>					
	Chem. elem. wt. %	O	Mg	Al	Si	Fe	Cu	Zn
	Spectrum Number							
As-annealed	1	7.1	3.8	73.3	2.8	2.3	2.1	8.6
	2	28.9	1.6	58.1	4.5	0.7	1.0	5.2
	3	14.2	2.6	68.7	1.5	1.7	3.1	8.2
	4	31.4	1.1	62.4	1.1	0.6	0.6	2.8
	5	32.8	2.1	57.9	2.1	0.5	0.8	3.8
1-pass ECAP	1	50.9	0.8	46.6	0.5	0.1	0.8	0.3
	2	25.1	1.3	71.5	0.6	0.2	1.1	0.2
	3	34.1	0.7	58.6	3.1	1.0	2.1	0.4
	4	35.0	1.0	62.0	0.2	0.2	1.1	0.5
	5	46.2	4.9	33.3	7.9	3.1	2.1	2.5
2-pass ECAP	1	42.6	0.7	53.2	0.9	0.3	1.7	0.6
	2	22.0	1.2	73.5	1.4	0.4	1.4	0.1
	3	10.7	0.5	84.9	1.8	0.3	1.5	0.3
	4	32.8	0.4	63.9	0.5	0.3	1.7	0.4
4-pass ECAP	1	11.1	1.2	82.8	2.2	0.2	1.6	0.9
	2	41.2	0.3	45.9	8.8	0.9	1.9	1.0
	3	13.4	3.6	53.0	3.3	5.4	15.5	5.8
	4	17.8	1.3	74.7	3.1	0.4	2.3	0.4
	5	6.1	1.5	87.8	1.4	1.0	1.9	0.3

### 3.4. Subsurface Deformation of AA7075

Subsurface regions of the samples have been examined using metallographic polished views prepared by sectioning the samples in the vertical plane parallel to the sliding direction and perpendicular to the top surface (Figure 14). These metallographic views distinguished at least two subsurface deformed layers such as (I) the severely deformed one below the worn surface and (II) the underlying layer, with the strain gradually reducing to zero in the base undeformed AA7075 metal. It may be noted that the total strain penetration depth, as well as layer I and II thicknesses, depended on AA7075's structural state and the type of the counterpart material. The layer thicknesses are most greatly changed when using ceramic balls.



**Figure 14.** Deformed layers below the worn surface obtained using balls made from 52100 steel (a,d,g,j),  $\text{Al}_2\text{O}_3$  (b,e,h,k) and  $\text{Si}_3\text{N}_4$  (c,f,i,l) balls. As-annealed (a–c), 1-pass (d–f), 2-pass (g–i), 4-pass (j–l) AA7075.

Layer I is rather thin when formed using the steel ball counterpart and contains some fraction of oxidized metal, while layer II is represented by AA7075 deformed by the friction force. Sliding with the alumina ball allowed us to increase the layer I thickness, as well as oxidize it more. Using the silicon nitride ball resulted in increasing the layer I thickness even faster. This layer contains oxidized regions as well as interlayers composed of oxides and non-oxidized metal. Layer II is not easy to observe but the shear deformation mode may be followed by particle streaks.

The layer I thicknesses obtained in sliding against steel and alumina balls may be somewhat increased on the ECAPed samples, while a much higher effect is observed in sliding the silicon nitride ball on the two-pass and four-pass ECAPed samples. Such a finding may be related to the above-discussed higher intensity of adhesion transfer on the silicon nitride ball.

The layer II thickness is reduced when using the steel ball (Figure 15b) on the ECAPed samples, but this situation is changed when using the ceramic balls instead. ECAPed samples demonstrate increased thicknesses of the deformed layers compared to that of the as-annealed one. The reason behind such a finding may be the generation of the adhesion transfer layer under conditions of enhanced stick-slip vibration.

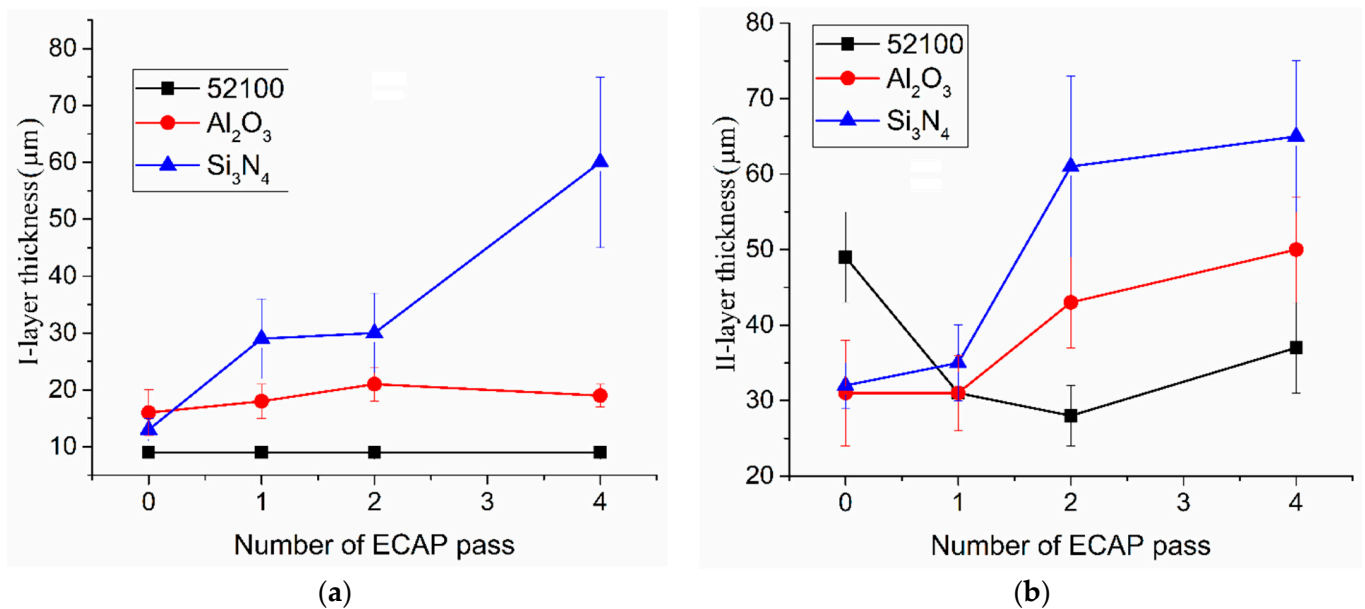


**Figure 15.** Effect of ECAP pass number and counterbody material on thickness of I layer severely (a) and II layer gradually (b) deformed of AA 7075 samples.

Summarizing the results of the experimental studies, we can conclude that several mechanisms may determine the wear of AA7075 samples:

1. Adhesive interaction between the ball and AA7075 samples, which also determines the transfer layer generation conditions.
2. Subsurface deformation of the samples with the following subsurface fracture, as well as the reversed transfer of material from the counterbody layer.
3. Mechanical vibrations of tribocoupling, which, through microimpacts on the surface, lead to more intensive hardening of the material and thereby accelerate its fracture.

The following conclusions about the wear of samples dependent on the counterbody material can be made:

1. The minimal wear of AA7075 samples during sliding against the steel ball is partly due to the lowest hardness of the material of 52100 steel itself, compared to Al<sub>2</sub>O<sub>3</sub> and Si<sub>3</sub>N<sub>4</sub>, i.e., harder ceramic counterbodies will mean more intensive abrasive wear.

2. The maximal wear of the AA7075 samples was observed in sliding against the Al<sub>2</sub>O<sub>3</sub> counterbody due to the high hardness of the counterbody material. On the other hand, the rationale may be the insufficiently effective formation of the reversed transfer layer.
3. The medium-intensity wear of AA7075 samples during sliding in pair with a Si<sub>3</sub>N<sub>4</sub> ball is due to the intensive formation of a reversed transfer layer, which acts as a protective coating. Despite the high hardness of the counterbody, this layer effectively protects the surface of the sample from the mechanical impact of the ball. It was also noticed that there were minor differences in wear among the ECAPed AA7075 samples in sliding against the silicon nitride ball, which may be explained by the generation of a thick layer I. Although not providing sufficiently strong bonding with the base material, this layer is capable of providing some protection against wear due to its fast restoration. In addition, a moderate level of run RMS (the average from the three balls) ensures less damage to this protective layer and, therefore, its higher stability throughout the entire friction.

To quantify the relationship between the sliding parameters and the mechanical characteristics of the AA7075 samples, the values of the correlation coefficients were determined for the measured characteristics (Tables 4–6).

**Table 4.** Correlation coefficients for comparing mechanical characteristics and sliding 52100/AA7075.

Parameters	Worn Surface Area	Adhesion Layer Thickness	AE Energy	AE F Median
CoF	−0.9	−0.89	0.97	0.73
runRMS	−0.89	−0.86	0.98	0.7
AE energy	−0.81	−0.76	-	0.56
AE F (median)	−0.92	−0.96	0.56	-
Yield strength (tension)	−0.9	−0.99	0.68	0.95
Ultimate tension strength	−0.89	−0.98	0.76	0.89

**Table 5.** Correlation coefficients for comparing mechanical characteristics and sliding Al<sub>2</sub>O<sub>3</sub>/AA7075.

Parameters	Worn Surface Area	Adhesion Layer Thickness	AE Energy	AE F Median
CoF	−0.95	−0.91	0.99	0.83
runRMS	−0.78	−0.86	0.7	0.98
AE energy	−0.92	−0.87	-	0.8
AE F (median)	−0.89	−0.94	0.8	-
Yield strength (tension)	−0.96	−0.93	0.99	0.86
Ultimate tension strength	−0.97	−0.96	0.96	0.93

**Table 6.** Correlation coefficients for comparing mechanical characteristics and sliding Si<sub>3</sub>N<sub>4</sub>/AA7075.

Parameters	Worn Surface Area	Adhesion Layer Thickness	AE Energy	AE F Median
CoF	−0.67	−0.95	0.82	0.99
runRMS	−0.63	−0.82	0.91	0.99
AE energy	−0.84	−0.76	-	0.85
AE F (median)	−0.62	−0.88	0.85	-
cYield strength (tension)	−0.94	−0.89	0.95	0.84
Ultimate tension strength	−0.88	−0.91	0.96	0.92

A direct correlation is observed between the AE signal parameters (AE energy, F<sub>median</sub>) and the CoF values, as well as the runRMS magnitude. Another example of such a direct

correlation is observed between the acoustic emission parameters (AE energy, AE median frequency) and tensile characteristics of the samples (UTS and YS). At the same time, an inverse correlation is observed between the AE signal parameters and wear of samples on the one side and the thickness of the adhesive transfer layer on the other side.

The YTS and UTS allow us to observe their inverse correlations with either wear or the adhesive transfer layer thickness. All the above-designated correlations of the AE signal parameters may result from structural states formed in the samples and somehow manifest in the friction and wear dynamics. It is also clear that the mechanical properties are related to the wear of the AA7075 samples.

#### 4. Conclusions

Tribological testing was carried out on AA7075 as-annealed and ECAPed samples to elucidate the phase and structural evolution of these materials in sliding with steel and ceramic counterparts.

In all considered cases, the use of ECAP made it possible to significantly reduce wear compared to the as-annealed samples. Minimal wear was achieved on the two-pass ECAP sample. Increasing the number of ECAP passes to four was not effective, since this resulted in enhanced wear of the samples.

The wear was reduced by a factor of 4.5, 3.8 and 2.3 on the ECAPed samples tested with the use of counterbody balls made from steel, alumina and silicon nitride, respectively, as compared to that of the as-annealed sample.

According to the data obtained, the key wear mechanisms of the AA7075 samples under dry-sliding friction conditions are determined by subsurface deformation and fracture of oxidized tribologically affected layers on AA7075.

An important factor of wear is the adhesion transfer of the AA7075 metal onto the counterbody's surface. The transfer and pulling out of the metal is more intense when using the ceramic counterparts, despite all balls having almost the same values of friction force.

The median frequency and energy of acoustic emission are sensitive to the effect of materials structure on dynamics of the friction and wear of AA7075 samples.

**Author Contributions:** Conceptualization, A.V.F.; Funding acquisition, A.V.F. and S.Y.T.; Supervision, A.V.F.; Writing—Review and Editing, A.V.F. and S.Y.T.; Writing—Original Draft, A.V.F. and S.Y.T.; Experimentation, A.V.F. and S.Y.T.; Data management, E.O.F.; Verification, E.O.F.; Project administration, A.V.F. All authors have read and agreed to the published version of the manuscript.

**Funding:** The work was performed under the government statement of work for ISPMS SB RAS, Project No. FWRW-2021-0006.

**Data Availability Statement:** The raw data supporting the conclusions of this article will be made available by the authors on request.

**Conflicts of Interest:** The authors declare no conflicts of interest.

#### References

1. Baydoğan, M.; Çimenoglu, S.; Kayali, E.S. A study on sliding wear of a 7075 aluminum alloy. *Wear* **2004**, *257*, 852–861. [[CrossRef](#)]
2. Rigney, D.A. Transfer, mixing and associated chemical and mechanical processes during the sliding of ductile materials. *Wear* **2000**, *245*, 1–9. [[CrossRef](#)]
3. Yang, Z.-R.; Sun, Y.; Li, X.-X.; Wang, S.-Q.; Mao, T.-J. Dry sliding wear performance of 7075 Al alloy under different temperatures and load conditions. *Rare Met.* **2022**, *41*, 1057–1062. [[CrossRef](#)]
4. Shanmughasundaram, P. Statistical analysis on influence of heat treatment, load and velocity on the dry sliding wear behavior of aluminium alloy 7075. *Mater. Phys. Mech.* **2015**, *22*, 118–124.
5. Bhatia, P.K.; Tiwari, S.; Yadav, G. Sliding Wear Behaviour of Aluminium Alloy 7075 Grade in Dry and Wet Conditions. *Int. J. Sci. Res. Dev.* **2016**, *4*, 525–527.
6. Zhang, P.; Xiong, Q.; Cai, Y.; Zhai, W.; Cai, M.; Cai, Z.; Zhu, J.; Gu, L. Dry fretting and sliding wear behavior of 7075-T651 aluminum alloy under linear reciprocating motion: A comparative study. *Wear* **2023**, *526–527*, 204942. [[CrossRef](#)]
7. Zhang, P.; Zeng, L.; Mi, X.; Lu, Y.; Luo, S.; Zhai, W. Comparative study on the fretting wear property of 7075 aluminum alloys under lubricated and dry conditions. *Wear* **2021**, *474–475*, 2021. [[CrossRef](#)]

8. Cai, Z.-B.; Zhu, M.-H.; Lin, X.-Z. Friction and wear of 7075 aluminum alloy induced by torsional fretting. *Trans. Nonferrous Met. Soc. China* **2010**, *20*, 371–376. [[CrossRef](#)]
9. Shen, M.X.; Cai, Z.B.; Peng, J.F.; Song, C.; Mo, J.L.; Shen, H.M.; Zhu, M.H. Dual-rotary fretting wear of 7075 alloy in media of oil and water. *Wear* **2013**, *301*, 540–550. [[CrossRef](#)]
10. Shen, M.X.; Zhu, M.H.; Cai, Z.B.; Xie, X.Y.; Zuo, K.C. Dual-rotary fretting wear behavior of 7075 aluminum alloy. *Tribol. Int.* **2012**, *48*, 162–171. [[CrossRef](#)]
11. Shen, M.-X.; Cai, Z.-B.; Mo, J.-L.; Peng, X.-D.; Zhu, M.-H. Local fatigue and wear behaviors of 7075 aluminium alloy induced by rotational fretting wear. *Int. J. Surf. Sci. Eng.* **2015**, *9*, 520–537. [[CrossRef](#)]
12. Mo, J.L.; Zhu, M.H.; Zheng, J.F.; Luo, J.; Zhou, Z.R. Study on rotational fretting wear of 7075 aluminum alloy. *Tribol. Int.* **2010**, *43*, 912–917. [[CrossRef](#)]
13. Cai, Z.; Zhu, M.; Shen, H.; Zhou, Z.; Jin, X. Torsional fretting wear behaviour of 7075 aluminium alloy in various relative humidity environments. *Wear* **2009**, *267*, 330–339. [[CrossRef](#)]
14. Peng, J.; Jin, X.; Xu, Z.; Zhang, J.; Cai, Z.; Luo, Z.; Zhu, M. Study on the damage evolution of torsional fretting fatigue in a 7075 aluminum alloy. *Wear* **2018**, *402–403*, 160–168. [[CrossRef](#)]
15. Mao, L.; Cai, M.; Liu, Q.; He, Y. Effects of sliding speed on the tribological behavior of AA 7075 petroleum casing in simulated drilling environment. *Tribol. Int.* **2020**, *145*, 106194. [[CrossRef](#)]
16. Abeens, M.; Muruganatham, R.; Arulvel, S. Friction-wear behavior of shot peened aluminium 7075-T651 alloy. *Indian J. Eng. Mater. Sci.* **2019**, *26*, 20–26.
17. Tang, M.; Zhang, L.; Shi, Y.; Zhu, W.; Zhang, N. Research on the Improvement Effect and Mechanism of Micro-Scale Structures Treated by Laser Micro-Engraving on 7075 Al Alloy Tribological Properties. *Materials* **2019**, *12*, 630. [[CrossRef](#)]
18. Chegini, M.; Shaeri, M.H. Effect of equal channel angular pressing on the mechanical and tribological behavior of Al-Zn-Mg-Cu alloy. *Mater. Charact.* **2018**, *140*, 147–161. [[CrossRef](#)]
19. Chegini, M.; Fallahi, A.; Shaeri, M.H. Effect of Equal Channel Angular Pressing (ECAP) on Wear Behavior of Al-7075 Alloy. *Procedia Mater. Sci.* **2015**, *11*, 95–100. [[CrossRef](#)]
20. Vafaenezhad, H.; Chegini, M.; Kalaki, A.; Serajian, H. Micromechanical Finite Element Simulation of Low Cycle Fatigue Damage Occurring During Sliding Wear Test of ECAP-Processed AA7075 Alloy. *Met. Mater. Int.* **2023**, *30*, 143–166. [[CrossRef](#)]
21. Yilmaz, T.A.; Totik, Y.; Senoz, G.M.L.; Bostan, B. Microstructure evolution and wear properties of ECAP-treated Al-Zn-Mg alloy: Effect of route, temperature and number of passes. *Mater. Today Commun.* **2022**, *33*, 104628. [[CrossRef](#)]
22. Elhefnawey, M.; Shuai, G.L.; Li, Z.; Zhang, D.T.; Tawfik, M.M.; Li, L. On achieving ultra-high strength and improved wear resistance in Al-Zn-Mg alloy via ECAP. *Tribol. Int.* **2021**, *163*, 107188. [[CrossRef](#)]
23. Elhefnawey, M.; Shuai, G.L.; Li, Z.; Zhang, D.T.; Tawfik, M.M.; Li, L. On dry sliding wear of ECAPed Al-Mg-Zn alloy: Wear rate and coefficient of friction relationship. *Alex. Eng. J.* **2021**, *60*, 927–939. [[CrossRef](#)]
24. Avcu, E. The influences of ECAP on the dry sliding wear behaviour of AA7075 aluminium alloy. *Tribol. Int.* **2017**, *110*, 173–184. [[CrossRef](#)]
25. Palacios-Robledo, D.; Fresneda-García, J.; Lorenzo-Bonet, E.; Guerra-Fuentes, L.; Deaquino-Lara, R.; Hernández-Rodríguez, M.A.L.; García-Sánchez, E. Tribological analysis in Al-Mg-Zn alloy casting processed through equal channel angular pressing, compared with Al-7075 T6 alloy. *Wear* **2021**, *476*, 203680. [[CrossRef](#)]
26. Zhao, Y.H.; Liao, X.Z.; Jin, Z.; Valiev, R.Z.; Zhu, Y.T. Microstructures and mechanical properties of ultrafine grained 7075 Al alloy processed by ECAP and their evolutions during annealing. *Acta Mater.* **2004**, *52*, 4589–4599. [[CrossRef](#)]
27. Shaeri, M.H.; Salehi, M.T.; Seyyedain, S.H.; Abutalebi, M.R.; Park, J.K. Microstructure and mechanical properties of Al-7075 alloy processed by equal channel angular pressing combined with aging treatment. *Mater. Des.* **2014**, *57*, 250–257. [[CrossRef](#)]
28. Kumar, S.R.; Gudimetla, K.; Venkatachalam, P.; Ravisankar, B.; Jayasankar, K. Microstructural and mechanical properties of Al 7075 alloy processed by Equal Channel Angular Pressing. *Mater. Sci. Eng. A* **2012**, *533*, 50–54. [[CrossRef](#)]
29. Mogonye, J.E.; Scharf, T.W. Tribological properties and mechanisms of self-mated ultrafine-grained titanium. *Wear* **2017**, *376–377*, 931–939. [[CrossRef](#)]
30. Deng, G.; Chong, Y.; Su, L.; Zhan, L.; Wei Pe Zhao, X.; Zhang, L.; Tian, Y.; Zhu, H.; Tsuji, N. Mechanisms of remarkable wear reduction and evolutions of subsurface microstructure and nano-mechanical properties during dry sliding of nano-grained Ti6Al4V alloy: A comparative study. *Tribol. Int.* **2022**, *169*, 107464. [[CrossRef](#)]
31. Deng, G.; Zhao, X.; Su, L.; Wei, P.; Zhang, L.; Zhan, L.; Chong, Y.; Zhu, H.; Tsuji, N. Effect of high pressure torsion process on the microhardness, microstructure and tribological property of Ti6Al4V alloy. *J. Mater. Sci. Technol.* **2021**, *94*, 183–195. [[CrossRef](#)]
32. Seenuvasaperumal, P.; Doi, K.; Basha, D.A.; Singh, A.; Elayaperumal, A.; Tsuchiya, K. Wear behavior of HPT processed UFG AZ31B magnesium alloy. *Mater. Lett.* **2018**, *227*, 194–198. [[CrossRef](#)]
33. Guo, H.; Fan, J.; Zhang, H.; Zhang, Q.; Wu, Y.; Li, W.; Dong, H.; Xu, B. The preparation and mechanical properties of nano-magnesium alloy bulks. *J. Alloys Compd.* **2020**, *819*, 153253. [[CrossRef](#)]
34. Chen, L.; Li, W.; Sun, Y.; Luo, M. Effect of microstructure evolution on the mechanical properties of a Mg-Y-Nd-Zr alloy with a gradient nanostructure produced via ultrasonic surface rolling processing. *J. Alloys Compd.* **2022**, *923*, 166495. [[CrossRef](#)]
35. Sankuru, A.B.; Ahirwar, V.; Ravisankar, B.; Kumares, B.S. Mechanical and wear behavior of room-temperature ECAPed Mg-4Li alloy. *Proc. Inst. Mech. Eng. Part C J. Mech. Eng. Sci.* **2024**, *238*, 2120–2130. [[CrossRef](#)]

36. Filippov, A.V.; Tarasov, S.Y.; Fortuna, S.V.; Podgornykh, O.A.; Shamarin, N.N.; Rubtsov, V.E. Microstructural, mechanical and acoustic emission-assisted wear characterization of equal channel angular pressed (ECAP) low stacking fault energy brass. *Tribol. Int.* **2018**, *123*, 273–285. [[CrossRef](#)]
37. Lin, R.; Liu, B.; Zhang, J.; Zhang, S. Microstructure evolution and properties of 7075 aluminum alloy recycled from scrap aircraft aluminum alloys. *J. Mater. Res. Technol.* **2022**, *19*, 354–367. [[CrossRef](#)]
38. Hembram, M.; Singh, P.; Kumar, N. High Strain Behaviour of Ultrafine-grained Aluminium Alloys Processed Through the Severe Plastic Deformation Techniques: A Review. *Metallogr. Microstruct. Anal.* **2022**, *11*, 684–703. [[CrossRef](#)]
39. Huang, K.; Logé, R.E. A review of dynamic recrystallization phenomena in metallic materials. *Mater. Des.* **2016**, *111*, 548–574. [[CrossRef](#)]
40. Sakai, T.; Belyakov, A.; Kaibyshev, R.; Miura, H.; Jonas, J.J. Dynamic and post-dynamic recrystallization under hot, cold and severe plastic deformation conditions. *Prog. Mater. Sci.* **2014**, *60*, 130–207. [[CrossRef](#)]
41. Imai, K.; Hase, A. Identification of Tribological Phenomena in Glass Grinding by Acoustic Emission Sensing. *Tribol. Online* **2022**, *17*, 86–96. [[CrossRef](#)]
42. Hase, A. In Situ Measurement of the Machining State in Small-Diameter Drilling by Acoustic Emission Sensing. *Coatings* **2024**, *14*, 193. [[CrossRef](#)]
43. Koga, T.; Hase, A.; Ninomiya, K.; Okita, K. Acoustic emission technique for contact detection and cutting state monitoring in ultra-precision turning. *Mech. Eng. J.* **2019**, *6*, 2187–9745. [[CrossRef](#)]
44. Savchenko, N.L.; Filippov, A.V.; Tarasov, S.Y.; Dmitriev, A.I.; Shilko, E.V.; Grigoriev, A.S. Acoustic emission characterization of sliding wear under condition of direct and inverse transformations in low-temperature degradation aged Y-TZP and Y-TZP-AL<sub>2</sub>O<sub>3</sub>. *Friction* **2018**, *6*, 323–340. [[CrossRef](#)]
45. Filippov, A.V.; Rubtsov, V.E.; Tarasov, S.Y.; Podgornykh, O.A.; Shamarin, N.N. Detecting transition to chatter mode in peakless tool turning by monitoring vibration and acoustic emission signals. *Int. J. Adv. Manuf. Technol.* **2018**, *95*, 157–169. [[CrossRef](#)]
46. Filippov, A.V.; Nikonov, A.Y.; Rubtsov, V.E.; Dmitriev, A.I.; Tarasov, S.Y. Vibration and acoustic emission monitoring the stability of peakless tool turning: Experiment and modeling. *J. Mater. Process. Technol.* **2017**, *246*, 224–234. [[CrossRef](#)]
47. Filippov, A.V.; Tarasov, S.Y.; Fortuna, S.V.; Podgornykh, O.A.; Shamarin, N.N.; Vorontsov, A.V. Wear, vibration and acoustic emission characterization of sliding friction processes of coarse-grained and ultrafine-grained copper. *Wear* **2019**, *424–425*, 78–88. [[CrossRef](#)]
48. Filippov, A.V.; Rubtsov, V.E.; Tarasov, S.Y. Acoustic emission study of surface deterioration in tribocontacting. *Appl. Acoust.* **2017**, *117*, 106–112. [[CrossRef](#)]
49. Tarasov, S.Y.; Filippov, A.V.; Kolubaev, E.A.; Kalashnikova, T.A. Adhesion transfer in sliding a steel ball against an aluminum alloy. *Tribol. Int.* **2017**, *115*, 191–198. [[CrossRef](#)]
50. Arık, H.; Erden, İ.O.; Aydın, M. Diffusion welding of Al- $\alpha$ -Si<sub>3</sub>N<sub>4</sub> composite materials. *Politek. Derg.* **2020**, *23*, 497–503. [[CrossRef](#)]
51. Laganá, S.; Mikkelsen, E.K.; Marie, R.; Hansen, O.; Mølhav, K. Direct bonding of ALD Al<sub>2</sub>O<sub>3</sub> to silicon nitride thin films. *Microelectron. Eng.* **2017**, *176*, 71–74. [[CrossRef](#)]

**Disclaimer/Publisher’s Note:** The statements, opinions and data contained in all publications are solely those of the individual author(s) and contributor(s) and not of MDPI and/or the editor(s). MDPI and/or the editor(s) disclaim responsibility for any injury to people or property resulting from any ideas, methods, instructions or products referred to in the content.